

Cyclotron Line Features from Near-Critical Fields II: on the Effect of Anisotropic Radiation Fields

Rafael A. Araya-Góchez

Laboratorio de Investigaciones Astrofísicas,
Escuela de Física, Universidad de Costa Rica,
San José, Costa Rica.

and

Alice K. Harding

Laboratory for High Energy Astrophysics,
NASA Goddard Space Flight Center, Greenbelt, MD 20771.

Subject headings: line: formation — magnetic fields — radiative transfer — stars:
neutron — X-rays: stars

ABSTRACT

We assess the impact of radiation anisotropy on the line shapes that result from relativistic magnetic Compton scattering in the low-density/high-field regime. A Monte Carlo implementation of radiation transport allows for spatial diffusion of photons in arbitrary geometries and accounts for relativistic angular redistribution. The cross section includes natural line widths and photon “spawning” from up to fourth harmonic photons. In our first paper we noted that even if the photon injection is isotropic a strongly anisotropic radiation field rapidly ensues. We now investigate the angular distribution of cyclotron spectra emerging from an internally irradiated magnetized plasma with a prescribed global geometry (either cylindrical or plane parallel) and the effects of anisotropic photon injection on the line shapes. Varying the input angular distribution permits a better understanding of the line formation process in more realistic scenarios where the radiative mechanisms are influenced by the intrinsic anisotropy of the field and by moderate relativistic beaming. In general, the line features are most pronounced along the directions of the anisotropic continuum

injection and tend to be weakened in other directions, relative to the line features resulting from an isotropic continuum injection. We find that the enhancements at the line wings of the fundamental, which appear prominently in the case of isotropic continuum injection, are strongly suppressed along the direction of anisotropy in the case of beamed continuum injection, regardless of geometry or beaming pattern.

1. INTRODUCTION

The most direct observational evidence of the magnetic field strength in neutron star sources is provided by X-ray cyclotron line features. Such quasi-harmonic spectral features are generated by scattering of resonant photons with the electrons embedded in the magnetosphere. The interaction is multiply resonant because the Dirac equation in the presence of a locally uniform magnetic field, \mathbf{B} , yields discrete perpendicular momentum eigenvalues (with $c = \hbar \equiv 1$): $(p_{\perp}/m_e)^2 = 2n(B/B_Q)$, but relativistic effects introduce a slight anharmonicity in the rest-frame resonant photon energies:

$$\omega_n/m_e = [(1 + 2nB'\sin^2\theta)^{1/2} - 1]/\sin^2\theta, \quad (1)$$

where $B' \equiv B/B_Q$ and $B_Q = m^2/e(c^3/\hbar) \simeq 44$ TG is the Q.E.D. field scale. As these energies depend non-trivially on the photon’s propagation angle with respect to the field, $\theta = \cos^{-1}(\hat{\mathbf{k}} \cdot \hat{\mathbf{B}})$, the emergent spectral features are heavily influenced by the angular distribution of resonant photons as well as by the spatial distribution of electron targets (i.e. plasma “geometry”) and by the scattering region’s orientation with respect to the magnetic field.

Cyclotron lines have been detected in a number of X-ray pulsar spectra (Nagase 1989, Mihara, 1995, Santangelo et al. 1999) and possibly also in the spectra of several Gamma Ray Bursts (Mazets *et al.* 1981, 1883 Murakami *et al.* 1988, Yoshida *et al.* 1991). While there is a broad consensus on the origin of the former objects, the origin of gamma ray bursts remains highly elusive. Line energies in X-ray pulsars typically fall in the range from 4 to 40 keV, indicating¹ scattering of electrons in magnetic fields of up to 3.5 TG. The case of transient X-ray pulsar

¹ Note that the standard interpretation of field strength through the cyclotron fundamental $\omega_{cyc} = m_e(B/B_Q)$ assumes a hydrostatic plasma and is not unique. Models assuming bulk motion of the scattering electrons (e.g. Baushev & Bisnovatyi-Kogan 1999) will produce a Doppler-shifted line center, but the narrowness of the lines is then difficult to accommodate.

A0535+26 with an 11 TG field ($\sim \frac{1}{4}B_Q$) represents the uppermost limit spectrally determined (Grove *et al.* 1995, Araya and Harding 1996a-b, Maisack *et al.* 1997)

X-ray pulsars are found in binary systems containing a neutron star. In high mass X-ray binaries (HMXRB), a tenuous accretion wind occurs from the massive companion onto the neutron star surface. Low mass systems have higher accretion rates and disks surrounding the neutron star (see van den Heuvel & Rappaport 1987, for a review). The plasma geometry depends on the mechanism for stopping the accretion flow at the surface of the star, which is not certain in either case. If shocks form due to radiation pressure in high luminosity sources (Basko & Sunyaev 1976, Davidson 1973, Wang and Frank 1982, Arons, Klein and Lea 1985, 1987) or through a collisionless plasma instability in the flow of low luminosity sources (Langer and Rappaport 1982), the geometry of the X-ray emitting region will be a quasi-cylindrical column. This situation sharply contrasts the case of flow stopping through Coulomb collisions with the ambient electrons and protons where atmospheres with scale heights of order $h \sim 200$ cm are expected (Mészáros *et al.* 1983, Harding *et al.* 1984). These possible pictures of the flow provide two idealized, ‘orthogonal’ geometric scenarios: plane parallel slabs and cylinders. One hopes that models of cyclotron line features may provide a sensible diagnostic to determine the geometry of the region where the lines form. This, in turn, could also help answer some important questions regarding the microphysics involved in the stopping and cooling of the flow.

Unfortunately, the production of theoretical cyclotron line features in an entirely self-consistent manner is a formidable task requiring the resolution of a coupled radiation-magnetohydrodynamic system (e.g., Arons, Klein and Lea 1987). Even simplified approaches pose extremely difficult problems so the solutions are typically attempted in piecemeal form. For cyclotron features produced in hard incident continua (as in this investigation) the work of Isenberg, Lamb and Wang (1997, Lamb *et al.* 1989, Wang *et al.* 1989, Wang, Wasserman and Salpeter 1988) and of Alexander and Mészáros (1989, Alexander, Mészáros and Bussard 1989) represent the state of the art calculations and are closely related to the models produced here (for a comparison, see Araya & Harding 1999 [hereafter AH99]).

Our results ensue from a hard incident continuum (photon number power index = -1) throughout the entire energy range. This is motivated mainly by GRB spectra although some

X-ray pulsars exhibit a fairly hard X-ray continuum at the characteristic cyclotron energy (i.e. X0115+634, X0331+53, 4U 1538-52 and even A0535+26 at 110 keV). A hard incident spectrum allows for an easier interpretation of several processes affecting the formation of the fundamental cyclotron line feature such as relativistic angular redistribution of resonant photons and photon spawning in which electrons excited to higher Landau states produce additional photons through cyclotron decay. The theoretical spectra thus generated greatly aid in the interpretation of real spectra formed in softer continua such as those belonging to some X-ray pulsars (where the effect of photon spawning is substantially weaker).

In AH99, we presented model cyclotron line features for isotropic photon continuum injection. It was noted then that radiation transport and resonant scattering efficiently induced a strongly anisotropic radiation field. Moreover, the radiation processes in very strong magnetic fields and the inherent anisotropy induced by the plasma geometry are unlikely to produce isotropic continuum emission except perhaps deep inside the accretion column or mound. In this paper, we offer a detail quantification of the emergent angular distribution for isotropically injected photons scattered off electrons with a thermal energy distribution parallel to the field, and expand the calculations to encompass the influence of anisotropic photon injection on the emergent cyclotron line features.

In §2 we present a synopsis of the model and its regime of validity. Motivation to the study of anisotropic photon injection and details of its implementation are presented in §3 This scheme is then employed to study the line formation process, the emergent spectral line shapes and the angular distribution of emergent radiation in §4

2. Model Synopsis

The cyclotron line spectra are produced in *irradiated* magnetized plasmas without internal photon sources and with *prescribed* thermodynamic conditions. The chief simplification in our treatment of the radiation transport problem is conformity with the high-field/low density regime. Vacuum polarization then determines the photon states, and collisional interactions may be ignored. We have quantified this and the statements below in AH99.

The relativistic magnetic Compton scattering cross section (Sina 1996, see AH99) includes natural line widths through the use of dressed electron propagators evaluated in the presence of a uniform magnetic field (Graziani 1993, Graziani, Harding & Sina 1996). The electron states that permit such construction are simultaneous eigenstates of the *Sokolov-Ternov* (1967) relativistic spin operator (see, e.g., Melrose & Parle 1983, Sina 1996) while the photon polarization states are the magnetized vacuum normal modes uncorrected for dispersion (Shabad 1976).

In the strong field limit, use of the normal photon modes yields mode-dependent cross sections which are not substantially different from one another and mode switching branching ratios strongly couple the two modes. Wang, Wasserman and Salpeter (1988) thus found that both normal modes, ϵ_{\parallel} and ϵ_{\perp} , have comparable mean free paths and contribute about equally to the spectral angular output distributions in slab geometries. This motivates the treatment of unpolarized photons.

Detailed consideration of ‘Landau-Raman’ scattering allows photon spawning from up to fourth harmonic photons with electron momenta sampled from a relativistic thermal energy distribution function

$$f_e(p)dp = N_{T_e} \exp \left\{ -\frac{(\sqrt{1+p_e^2} - 1)}{T_e} \right\} dp$$

where T_e is the (one dimensional) parallel electron temperature, and N_{T_e} , the normalizaton. Regarding the Landau level populations, one need not consider detailed equilibrium in plasmas which are tenuous and cool relative to the cyclotron energy: For sub-critical fields, the radiative cyclotron de-excitation rate (Latal 1986), $\nu_r \simeq 2._{+15} B_{12}^2 \text{ sec}^{-1}$, is very large compared with the collisional rate (Bonazzola, Heyvaerts and Puget 1979), $\nu_c = 5._{+8} (n_e/1.0_{+21} \text{ cm}^{-3}) B_{12}^{-3/2} \text{ sec}^{-1}$. Thus, all electrons may be safely assumed to be in the ground Landau level initially.

In spite of the tenuous environment, a thermal characterization is justified by the resonant behavior of the magnetic Compton scattering cross section which ensures high optical depth in the line core and strong photon-electron coupling through multiple resonant scattering. An estimate for the equilibrium electron temperature, obtained from non-relativistic numerical simulations by Lamb, Wang and Wasserman (1990), also yields consistent results for hard continua (AH99): $T_e \simeq \frac{1}{4} \omega_{\text{cyc}}$, $\alpha_{\text{eff}} \sim -1$, $\tau \gg 1$, where $\omega_{\text{cyc}} = m_e(B/B_Q)$ is the nominal cyclotron frequency and α_{eff} the effective power law index at the line. Thus, in our calculations we take $T_e = 5.1 \text{ keV}$ for

$B' = 0.04$, $T_e = 12.8$ keV for $B' = 0.1$, $T_e = 31$ keV for $B' = 0.24$.

The Monte Carlo implementation for photon injection, propagation, and scattering permits the spatial diffusion of photons from arbitrary photon source functions and in arbitrary plasma geometries. A relativistic photon angle redistribution function, accurate for core scattering events that leave the electron back in the ground level and approximate otherwise, is also used to allow for angular diffusion.

The “absorption” approximation used to sample angular redistribution and to choose the target electrons’ initial momenta in the majority² of scattering events is strictly valid as long as the resonant part of the cross section dominates. Accuracy in the line core is warranted but not in the wings where the full scattering cross section provides a better description.

Each spectrum is formed by unbiased injection of fifty thousand individual photons from N_E identical energy bands evenly distributed throughout the spectral range. This is followed by re-processing of each photon through scattering and subsequent collection of the escaping radiation in a similar energy grid. To avoid poor statistics at high energies, photons are injected from a flat spectrum and are assigned spectral weights.

Two geometries for the scattering region are considered: plane parallel slab (with the magnetic field parallel to the slab’s normal vector) and cylindrical (with the field parallel to the cylinder axis). Because of axial symmetry, the $\hat{\mathbf{1}}_z$ direction is oriented along the magnetic field \mathbf{B} . A continuum photon spectrum is incident from a source at the slab midplane or from the cylinder axis. Internally, the source code keeps track of $N_\mu = 20$ equally spaced values of $\mu \equiv \hat{\mathbf{k}} \cdot \mathbf{B} \in [-1, 1]$, the cosine of the viewing angle to the field, and of $N_E = 80$ energy bins with $k^0 \in [\omega_{min}, \omega_{max}]$. The injected and escaping photons are accumulated into four ranges of $\mu \in [0, 1]$, and angle-dependent spectra are formed by considering the number of emerging photons in each of the N_E energy bins. The Thomson optical depth of the plasma in the line forming region, the electron temperature and the spectral index of injected photons are prescribed.

²except at the last scattering event where the program makes use of more accurate algorithms to “double-check” that the photon should indeed escape.

3. Anisotropic Photon Injection

3.1. Motivation

Our primary motivation for investigating the effect of anisotropic continuum photon distributions on cyclotron line formation is the fact that almost all radiation processes in the strong magnetic fields of X-ray pulsars produce anisotropic radiation. Such anisotropy results from the strong angle dependence of the magnetized cross sections for Compton scattering and radiation rates for cyclotron and bremsstrahlung (e.g. Meszaros 1992). A continuum spectrum resulting from inverse Compton scattering would have a flux peak along the magnetic field direction, while for cyclotron emission from non-relativistic electrons the radiation peaks perpendicular to the field direction.

In addition to the expected anisotropy of continuum radiation processes, the cyclotron scattering process itself produces anisotropies through angular redistribution. In AH99, we found that isotropically injected photons scattering through a slab were preferentially beamed along the magnetic field direction normal to the slab. Meanwhile, isotropically injected photons scattering through a cylinder were beamed across the field direction. Thus, it is of intrinsic interest to explore the interplay between continuum anisotropy and scattering-produced anisotropy.

Since the opening angle for the injection is very small (see Eq [3]), the injection imitates the behavior of a δ -function for injection at angles parallel and perpendicular to the \mathbf{B} -field. The study of beamed injection in these two limiting cases will help to understand, interpret and ‘de-convolve’ the linear coupling of the cyclotron line shapes to the anisotropies of the radiation field.

The essential features of cyclotron line formation in the high-field/low density regime were discussed in AH99. In that paper we commented on the effect of increasing the magnetic field strength from $\approx .04B_Q$ to $\approx .24B_Q$. Because the nominal estimate of electron temperature scales directly with field strength, the features at near-critical fields generally become very broad. Moreover, although there may have been some expectation that at large fields low harmonic features would resemble the fundamental line, this was not born out in our numerical results because the angular redistribution function is inherently different for photons at the fundamental cyclotron energy. At low fields, $n \neq 1$ cyclotron line features are ‘absorption-like’ because the

electrons prefer to de-excite in single perpendicular momentum quanta thus spawning photons just short of the fundamental cyclotron energy. The dynamics of line formation is thus most complicated at the fundamental energy. In hard continua, photon spawning produces very significant, broad line wings which distinguishes the fundamental feature from all others.

3.2. Model Parameter Selection

All of the runs have a continuum optical depth $\tau_c = 1..3$. The incident photon number spectra depend on energy through a simple power-law

$$\frac{dN_\omega}{d\omega d\mu} = \Theta(\theta) \times \omega^\alpha \quad \text{with } \alpha = -1. \quad (2)$$

The angular dependence of the injected spectra, $\Theta(\mu)$, models three limiting cases: isotropic, cone beam (where individual photons are injected along the magnetic field) and fan beam (with photons injected perpendicular to the \mathbf{B} -field). We choose a Lorentzian function for the probability distribution of angular injection of photons because it allows a simple implementation of the anisotropic injection process through Monte Carlo sampling. The functional form of the angular distribution is

$$\Theta(\theta) = \frac{1}{\pi} \left(\frac{(2/\theta_{op})}{\left[\frac{2}{\theta_{op}}(\theta - \theta_0) \right]^2 + 1} \right), \quad (3)$$

where: $\theta_{op} = 10^0$ is the opening angle, or ‘half-width’ of the cone or fan, and where θ_0 is the center of the distribution: $\theta_0 = 0$ for the cone and $\theta_0 = \pi/2$ for the fan distribution.

4. Results and Discussion

As we have already emphasized, the angular dependence of the emerging photons in both geometries show noticeable departures from isotropy even when the injection is done isotropically (examine the top graphs in Figs. 2, 4, 6, 8, 10, and 12). The most plausible causes for this are the spatial bias induced by the geometry of the scattering region and the relativistic forward beaming of scattered photons in the direction of the intermediate electron’s momentum \mathbf{p}_e (i.e. parallel or anti-parallel to the \mathbf{B} -field). As expected, slab geometries show the strongest anisotropy: The

effect of forward scattering (along the field) added to the most favorable photon escape conditions at small angles to the field account for this result.

As a rough measure of anisotropy we define a benchmark ratio: the escaping photon number flux @ $\mu \simeq 1$, to photon number flux @ $\mu \simeq 0$, $\mathfrak{R}_{\text{Geometry}}^{\text{Injec.bias}}$, with a super-index indicating the injection bias (C for cone, F for fan and I for isotropic) and a sub-index indicating geometry (sl for slab and cy for cylinder).

For plane parallel slabs and isotropic injection at the lower field strengths ($B'=.04$ and $\tau_c = 1._{-3}$), the ratio of photon number flux in the $\mathbf{1}_z$ direction to the flux perpendicular to $\mathbf{1}_z$ is $\mathfrak{R}_{\text{sl}}^{\text{I}} = 3.8$. For the cylinder, this same ratio is $\mathfrak{R}_{\text{cy}}^{\text{I}} = .60$ and the radiation escapes preferentially in the direction of least optical depth ($\mu \rightarrow 0$).

The anisotropy of the escaping radiation increases with optical depth (Araya 1996). For the slab (@ $B'=.04$ and $\tau_c = 3._{-3}$), $\mathfrak{R}_{\text{sl}}^{\text{I}} = 6.0$, but remains about the same for the cylinder, $\mathfrak{R}_{\text{cy}}^{\text{I}} = .64$, since the depth in the parallel direction is already large for this geometry.

In larger fields, the emerging photon anisotropy for slab remains about constant (@ $\tau_c = 1._{-3}$, $B' = 0.24$); $\mathfrak{R}_{\text{sl}}^{\text{I}} = 3.3$, and decreases slightly for the cylinder: $\mathfrak{R}_{\text{cy}}^{\text{I}} = .46$. This may seem surprising at first: For $B' = .24$ and $T_e = \frac{1}{4}B' = 31$ keV, one would expect stronger forward beaming from the mildly relativistic electrons of the plasma. However, the resonance profiles are stronger at lower fields (AH99). This seems to play a more dominant role in the angular biasing than does the relativistic forward beaming in this parameter space.

Let us examine next the effect of **beamed photon injection** (all fluxes will now correspond to a continuum optical depth $\tau_c = 1._{-3}$). For *cone* injection at the lower fields ($B' = .04$) our benchmark ratios are (Fig.2): $\mathfrak{R}_{\text{sl}}^{\text{C}} = 1.2_{+3}$ and $\mathfrak{R}_{\text{cy}}^{\text{C}} = 1.7_{+2}$, and for fan beam injection (Fig.4): $\mathfrak{R}_{\text{sl}}^{\text{F}} = 0.76$ and $\mathfrak{R}_{\text{cy}}^{\text{F}} = 0.12$. Clearly, cylinder geometries hinder large numbers of photons from emerging at small angles even if all the photons are injected there (cone injection) and the same can be said for spectra seen at large angles from slabs with fan beam injection.

However an unexpected result is now apparent; the scattering of photons injected perpendicular to the field tends to make these radiation field ratios more isotropic while the opposite happens for cone injection (note that the benchmark ratios are a **rough** measure of

isotropy; for a better description refer to the figures for the exact angular dependence of the emergent radiation). If relativistic scattering along the field direction is the cause of this behavior, then this trend should be stronger for the higher fields.

The ratios for parallel to perpendicular photon number flux at higher fields are: $\mathfrak{R}_{\text{sl}}^{\text{C}}(.10) = 1.4_2$, $\mathfrak{R}_{\text{cy}}^{\text{C}}(.10) = 6.8$ (Fig.6) and $\mathfrak{R}_{\text{sl}}^{\text{C}}(.24) = 1.1_2$, $\mathfrak{R}_{\text{cy}}^{\text{C}}(.24) = 4.2$ (Fig.10), for cone injection and $\mathfrak{R}_{\text{sl}}^{\text{F}}(.10) = .48$, $\mathfrak{R}_{\text{cy}}^{\text{F}}(.10) = 4.5_{-2}$ (Fig.8) and $Re_{\text{sl}}^{\text{F}}(.24) = .47$, $\mathfrak{R}_{\text{cy}}^{\text{F}}(.24) = 4.3_{-2}$ (Fig.12), for fan injection. Thus, note that our conjecture regarding the effect of relativistic scattering proves to be wrong: Fan beam injection at larger fields yield emerging spectra that are beamed along the perpendicular direction to the field, while the emerging radiation from cone injection is more isotropic!

Again we turn to the line profiles for an explanation. The fact that the total line profiles are higher at lower fields partially explains the observed behavior. Moreover, one may now attempt to find further causes for the hindering of the relativistic beaming. As was pointed out by Lamb et al (1989) for low fields in the non-relativistic limit, photons are removed from the incident spectrum at higher harmonic energies (see the branching ratios in AH99) at rates $\propto \sin^{2(n-1)}\theta$ and the spawned photon contribution is injected preferentially along the field $\propto 1 + \cos^2\theta$. This trend for angular redistribution (*modulo* relativistic corrections) is borne out qualitatively in our low field models. In higher fields the higher harmonic photons are not removed from the spectrum but are redistributed with similar angular dependencies (as derived from the cross sections in the rest-frame of the initial electron and in the ‘0p-frame’ of the intermediate electron (see Eqs: [57] and [59] of AH99), due to the preference for $0 \rightarrow n \rightarrow 0$ scattering.

The emergent spectra are shown in Figs. 1, 3, 5, 7, 9, and 11. Because the spectra are constrained by limited statistics, photon depletion at line center is unavoidable with the limited samples. Crosses indicate parts of the spectrum where photon depletion has occurred.

First, observe that in order to obtain an absorption dip for the first harmonic, the observer must see the spectra at an angle where injection has taken place: along the \mathbf{B} -field for cone injection or perpendicular to \mathbf{B} for fan injection. Moreover, beginning with Fig. [1], notice that by injecting the photons parallel to the field (cone injection) in a slab geometry, the broad line wings that occurred at small angles in the isotropic injection case disappear. Instead, the feature

at the fundamental resonant energy is absorption-like for small angles and at large angles it yields an emission line! (somewhat resembling the case of isotropic-injection in cylindrical-geometry). In addition note that for a cone injected slab the features at large angles are produced mostly by photons scattered out of small angles and that there is no replenishing of these photons, so that exaggerated features are expected. Thus, *the disappearance of the broad line wings for $\mu \sim 1$ suggests that these are formed by angular redistribution from $\mu \sim 0$.*

Recall from our discussion above that these spectra (cone injected slabs) have *strong* beaming along the \mathbf{B} -field. At lower fields the beaming is strongest. On the other hand, note that fan injected slabs at lower fields have the most isotropic emergent radiation field; this fact should make their spectra easier to interpret. The line wings are strongest in this case. An absorption-like line can be seen now for large viewing angles (i.e. the fundamental at $\mu < .25$). These two observations also suggest redistribution out of the injected pattern and into the solid angle space with less photon occupation relative to the continuum. The line wings for $\mu \sim 1$ are exaggerated because the continuum is low there. Alternatively, there is almost twice as much $\mathbf{1}_z$ flux bias in the isotropic injection case and the line wings at small angles are less prominent. This lends further support to our proposal regarding the connection between angular redistribution and the formation of the line wings.

Cone injected cylinders show strengthened signatures at the fundamental energy for $\mu > .25$, compared to the isotropically injected case (Fig.1). However, for small angles the line wings are depleted. Redistribution out of the cone accounts for the weakening of the line wings in cylinders as well. Fewer photons are scattered back into the small angles than are scattered out. The fan injected cylinders, Fig.3, exhibit a reverse trend: Line wings dominate except for $\mu \sim 0$ where there is virtually no feature at the fundamental for $B' = .04$. Although this is noteworthy, it is very unique to the parameter space of that particular model.

Higher field plots show a general trend of broadening in all the lines due to the higher temperatures required for detailed balance of cyclotron cooling and heating rates (Lamb, Wang, Wasserman 1990). For $B' = .24$, the extremely broad line wings in the isotropic injection case overwhelm the continuum at small angles in slabs. Again these wings completely go away when the photons are injected in a cone beam and an absorption-like line for $\mu \sim 0$ appears as it did in

lower fields.

Lastly, the higher field spectra exhibit a feature with strong asymmetry at the fundamental energy. This is a reflection of having *step*-like profiles at large angles due to the relativistic cut-off energy, in addition to lesser relative ratio between the profiles throughout the angle range. The profiles at lower fields show a ‘cusp’ at this energy and thus, the profile changes rapidly on either side of the cut-off energy. The profile at higher fields shows no such cusp; instead there is a sharp drop for energies beyond the relativistic cut off (Araya 1996, Araya & Harding 1999).

5. Conclusion

This study has illustrated that the angular distribution of the incident radiation has important effects on the emergent cyclotron line spectra. There is a profound interplay between the incident photon angular distribution and the geometry of the scattering region. In general, the line features are most pronounced along the directions of the anisotropic continuum injection and tend to be weakened in other directions, relative to the line features resulting from an isotropic continuum injection. We find that the enhancements at the line wings of the fundamental, which appear prominently in the case of isotropic continuum injection, are strongly suppressed along the direction of anisotropy in the case of beamed continuum injection, regardless of geometry or beaming pattern.

The absence of line wings at the fundamental may thus be an indicator of non-isotropic continuum radiation. These trends are strong enough that phase resolved spectral studies of observed cyclotron line features of X-ray pulsars may be able to identify the continuum anisotropy orientation relative to the direction of maximum optical depth of the scattering region. It thus may be possible to obtain information about the continuum emission mechanism from the shapes of the observed cyclotron lines in these sources.

We would like to thank Dr. R. Sina for supplying the code to calculate the cross section using Sokolov-Ternov electron wavefunctions, and Dr. A. Szalay for allowing us access to the supercomputer resources at the Johns Hopkins University.

REFERENCES

- Alexander, S.G., Meszaros, P. 1989, Ap.J., 344, L1.
- Alexander, S.G., Meszaros, P., Bussard, R. 1989, Ap.J., 342, 928.
- Alexander, S.G., Meszaros, P. 1990, Ap.J., 372, 554.
- Araya, R.A. 1996, Ph.D. Thesis, Johns Hopkins University.
- Araya, R.A., Harding A.K. 1996, Ap.J.Lett., 463, L33.
- Araya, R.A., Harding A.K., A&A Supp. Ser. 1996, 120, 183.
- Araya, R.A., Harding A.K. 1999, Ap.J., 517, 334.
- Arons, J., Klein, R. and Lea, S. 1985 in Plasma Penetration in Magnetospheres, eds N. Kylafis *et al.* (Crete Univ. Press) p. 141.
- Arons, J., Klein, R. and Lea, S. 1987, Ap.J., 312, 666.
- Basko, M.M. & Sunyaev R.A. 1975, A&A, 312, 666.
- Baushev, A.N. & Bisnovatyi-Kogan G.S. 1999, Ast.Rep. 43, 241.
- Basko, M.M. & Sunyaev R.A. 1976 M.N.R.A.S. 175, 395.
- Bildstein, L., *et al.* 1997 Ap.J.Supp., 113, 367B.
- Bonazzola, S., Heyvaerts J. and Puget J., 1979. A & A, 78, 53.
- Bulik, T. *et al.* 1992, Ap.J., 395, 564B.
- Bulik, T. 1993, Ph.D. Thesis, Pennsylvania State University.
- Bulik, T. *et al.* 1996, Ap.J., 444, 405.
- Bussard, R.W. 1980, Ap.J., 237, 970.
- Bussard, R.W., Alexander, S.B., Meszaros, P. 1986, Phys. Rev. D, 34, 440.
- Davidson K. 1973, Nature, 246, 1.
- Dittrich W., and Reuter M. 1984, Effective Lagrangians In Quantum Electrodynamics, Springer-Verlag Lecture Notes in Physics No 220.
- Graziani, C. 1993, Ap.J., 412, 351.
- Graziani, C., Harding, A.K., Sina, R. 1995, Phys.Rev.D, 51, 7097.
- Grove, J.E., Strickman, M.S., Johnson, W.N., Kurfess, J.D., Kinzer, R.L., Starr, C.H., Jung, G.V., Kendziorra, E., Kretschmar, P., Maisack, M., Staubert, R. 1995, Ap.J., 438, L25.
- Harding, A. K., Mészáros, P., Kirk, J. G. & Galloway, D. 1994, ApJ, 278, 369.
- Isenberg, M., Lamb, D., Wang, J. 1997, ApJ, 505, 688.
- Itzykson, C., and Zuber, J.B., 1982, Quantum Field Theory, (McGraw-Hill Co).
- Lamb, D.Q., Wang, J.C.L., Wasserman, I.M. 1990, Ap.J., 363, 670.
- Lamb, D., Wang, J., Loredo, T., Wasserman, I., Fenimore, E., 1989, in Proc 14th Texas Symp. on Relativistic Astrophysics Ed E. Feynves (New York: Ann NY Acad. Sci.), 571, 460
- Lamb, F.K., Pethick, C.J. and Pines, D. 1973, Ap.J., 184, 271.
- Langer, S.H. and Rappaport, S. 1982, ApJ, 257, 733.
- Maisack, M., Grove, E., Kendziorra, E., Kretschmar, P., Staubert, R., Strickman, M. 1997, A& A, 325, 212.
- Melrose, D.B., Aust J. Phys., 1983, 36, 775.
- Melrose, D.B., Parle, A.J., Aust J. Phys., 1983, 36, 755.

- Mészáros, P. 1992, "High Energy Radiation from Magnetized Neutron Stars" (Chicago: Univ. of Chicago Press).
- Mészáros, P. *et al.* , 1983, Ap.J., 266, L33.
- Mészáros, P., Nagel, W. 1985, Ap.J., 298, 147
- Mészáros, P., Nagel, W. 1985, Ap.J., 299, 138
- Mihalas, D. 1978, Stellar Atmospheres (Freeman: 2nd Ed).
- Mihalas, D. & Mihalas, B. 1984, Foundations of Radiation Hydrodynamics, (Oxford University Press).
- Mihara, T. 1995, Ph.D. Thesis, University of Tokyo.
- Nagase F. 1989, Publ. Astron. Soc. Japan 41, 1.
- Nagel, W. 1981, Ap.J., 251, 278
- Orlandini, M et al. 1999, ApJ, 523, L85.
- Ostriker and Gunn 1969, ApJ., 157, 1395.
- Shabad, A.E. 1976, Ann. of Phys., 90, 166.
- Schwinger, J. 1951, Phys. Rev. D, 82, 664.
- Sina, R. 1996, Ph.D. Thesis, University of Maryland.
- Sokolov, A. A., and Ternov, I.M., 1968, Synchrotron Radiation, (New York: Pergamon)
- Wang, J.C.L., Wasserman, I.M., Salpeter, E.E. 1988, Ap.J.S., 68, 735.
- Wang, J.C.L., *et al.* 1989, Phys. Rev. Lett., 63, 1550.
- Wang, Y.M. and Frank, J. 1982, A&A, 93, 255.
- Wang, Y.M. and Robertson, J.A., 1985, Ap.J. 299, 85.
- Woltjer, L., 1964, "X-Rays from Type I Supernova Remnants", Ap.J., 140, 1309.
- Wood, K. *et al.* , 1986, in: Gamma-Ray Bursts, ed. E.P. Liang and V. Petrosian (AIP, New York) p. 16.
- Yoshida, A. *et al.* , 1992, Proc. Los Alamos Workshop on Gamma Ray Bursts "Gamma-Ray Bursts: Observations, Analyses and Theories" ed. C. Ho, R.I. Epstein & E.E. Fenimore (Cambridge Univ. Press).

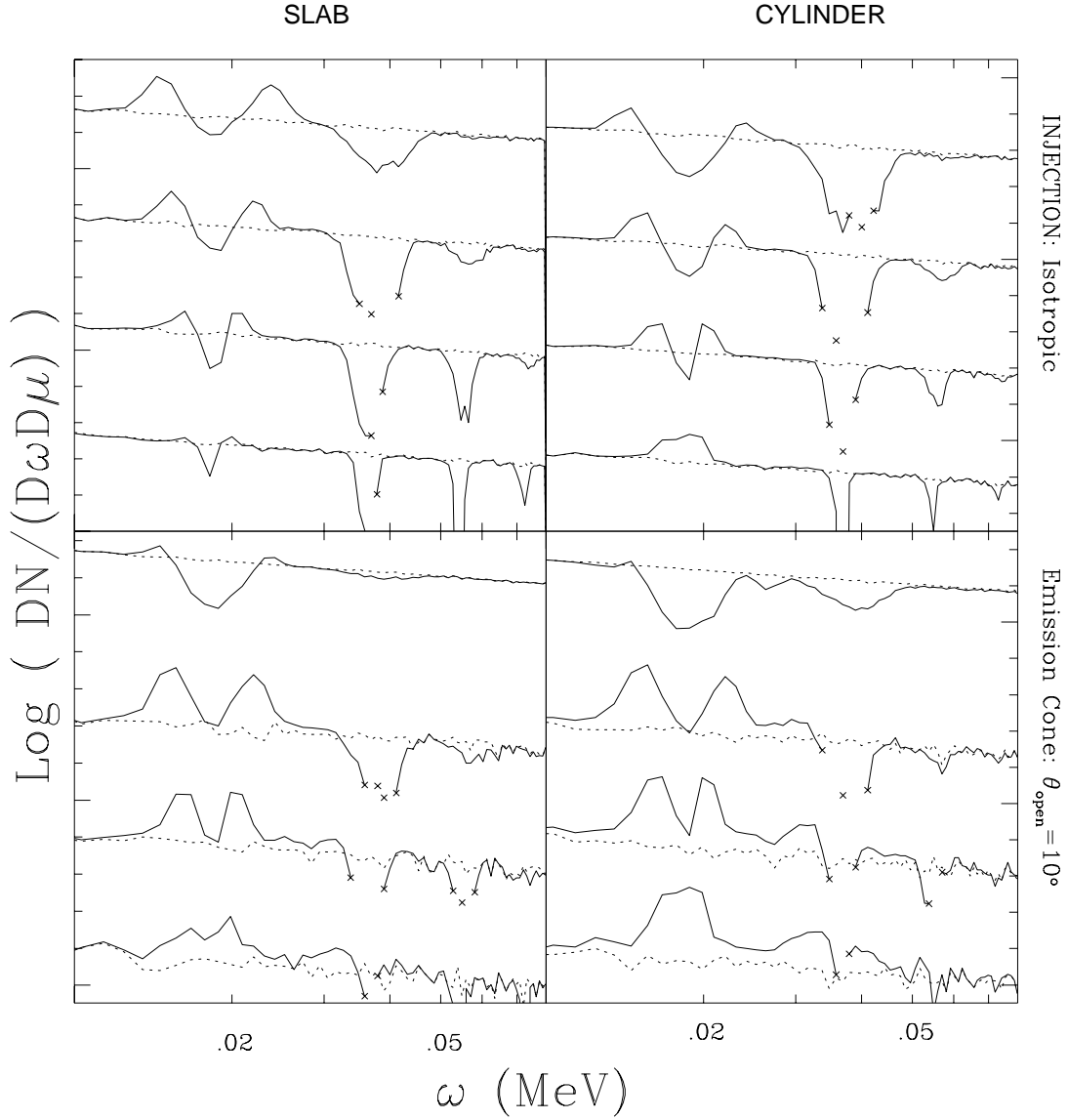


Fig. 1.— **Comparison between cone and isotropic injection for slab and cylindrical geometries.** The magnetic field strength is $B' = .04$ (1.7TG). Each plot shows angle dependent model photon spectra. On each quadrant, the bottom plot is the spectrum emerging from $\mu < .25$, followed by spectra from $.25 < \mu < .50$, from $.5 < \mu < .75$ and from $\mu > .75$ for the top plot. Each run results from 50 thousand photons injected isotropically, for the top plots, or within a lorentzian cone with opening angle $\theta_{op} = 10^\circ$ for the bottom plots. **Dotted line:** injected continuum: power law with $\alpha = -1$. **Solid line:** output scattered spectrum. **Crosses:** areas where photon depletion has occurred, the model points are indicated as crosses for ease of reading. $\tau_c = 1 \times 10^{-3}$, $T_e = \frac{1}{4} \omega_{cyc}$ The flux normalization is arbitrary. These are local spectra emitted near the neutron star surface and do not include General relativistic effects such as red shift or light bending.

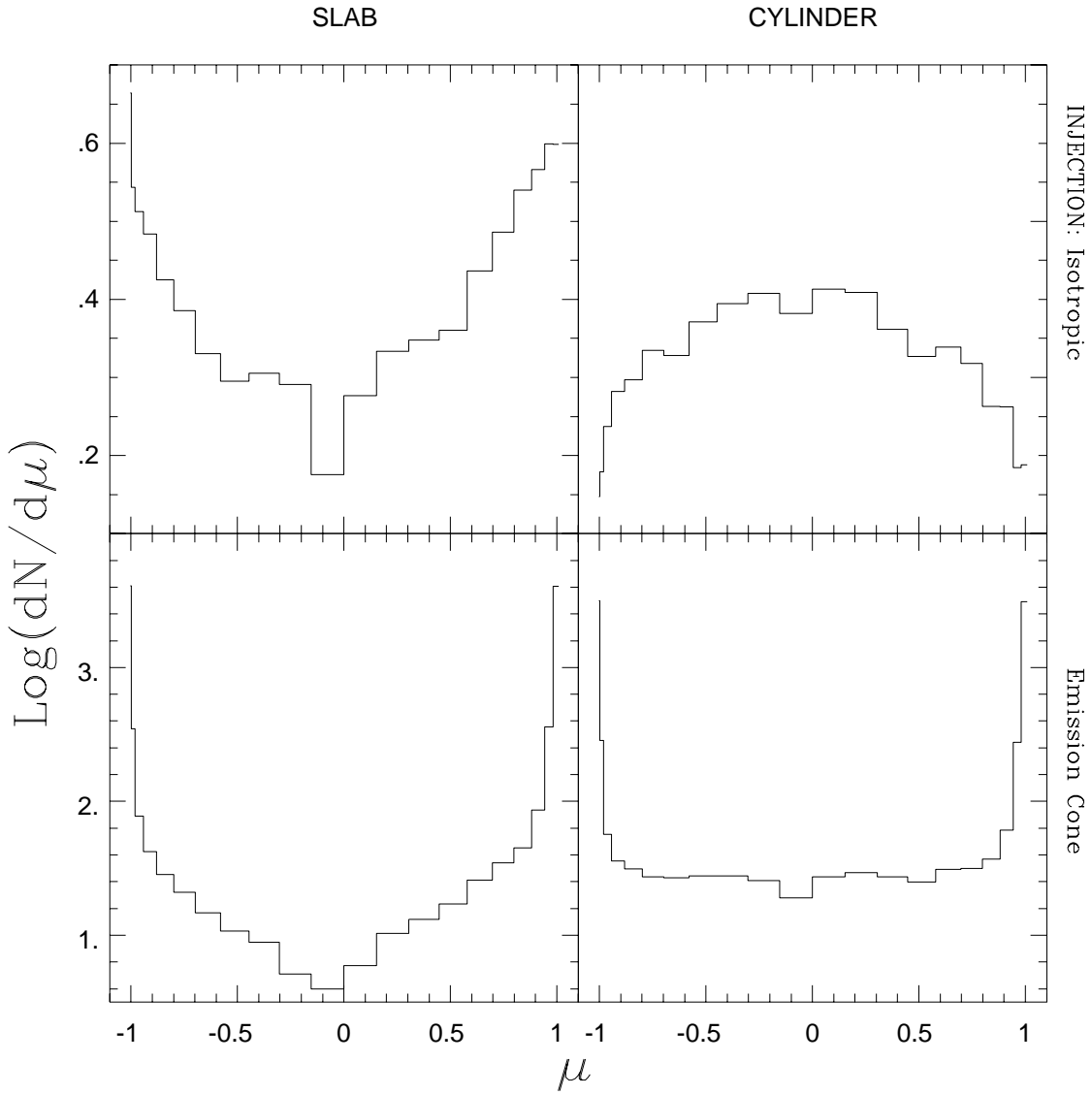


Fig. 2.— **Comparison of emergent angular distributions for cone and isotropic injections in slab and cylindrical geometries.** The parameters are identical with those of the preceding figure.

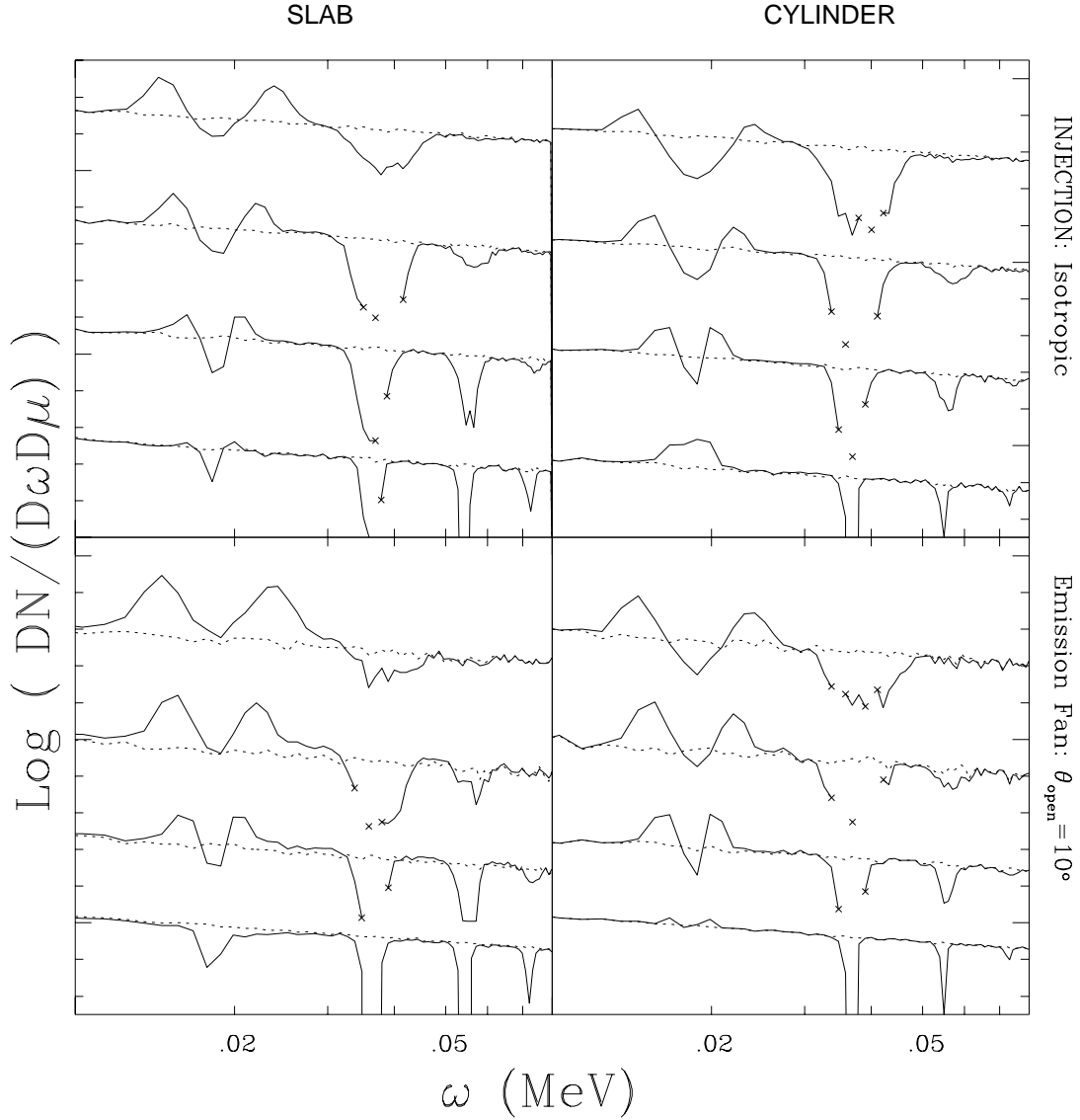


Fig. 3.— **Comparison between fan and isotropic injection for slab and cylindrical geometries.** The magnetic field strength is $B' = .04$ (1.7 TG). Each plot shows angle dependent model photon spectra. On each quadrant, the bottom plot is the spectrum emerging from $\mu < .25$, and the top plot shows the spectrum from $\mu > .75$, with similar binning in between. Each run results from 50 thousand photons injected isotropically, for the top plots, or within a lorentzian fan (injection perpendicular to \mathbf{B}) with opening angle $\theta_{op} = 10^\circ$, for the bottom plots. **Dotted line:** injected continuum: power law with $\alpha = -1$. **Solid line:** output scattered spectrum. **Crosses:** areas where photon depletion has occurred, the model points are indicated as crosses for ease of reading. $\tau_c = 1 \times 10^{-3}$, $T_e = \frac{1}{4}\omega_{cyc}$ The flux normalization is arbitrary.

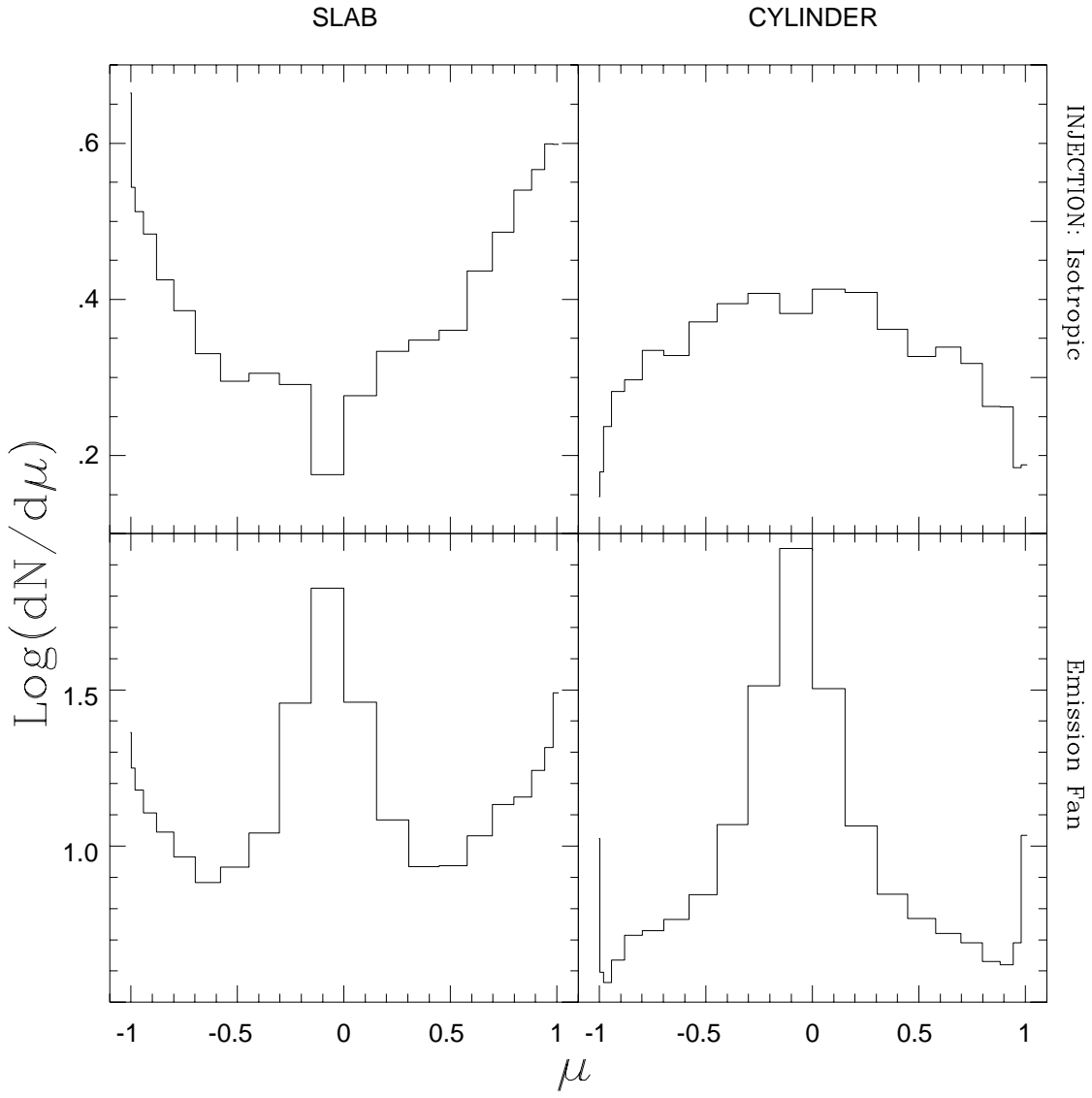


Fig. 4.— Comparison of emergent angular distributions for fan and isotropic injections in slab and cylindrical geometries. The parameters are identical with those of the preceding figure.

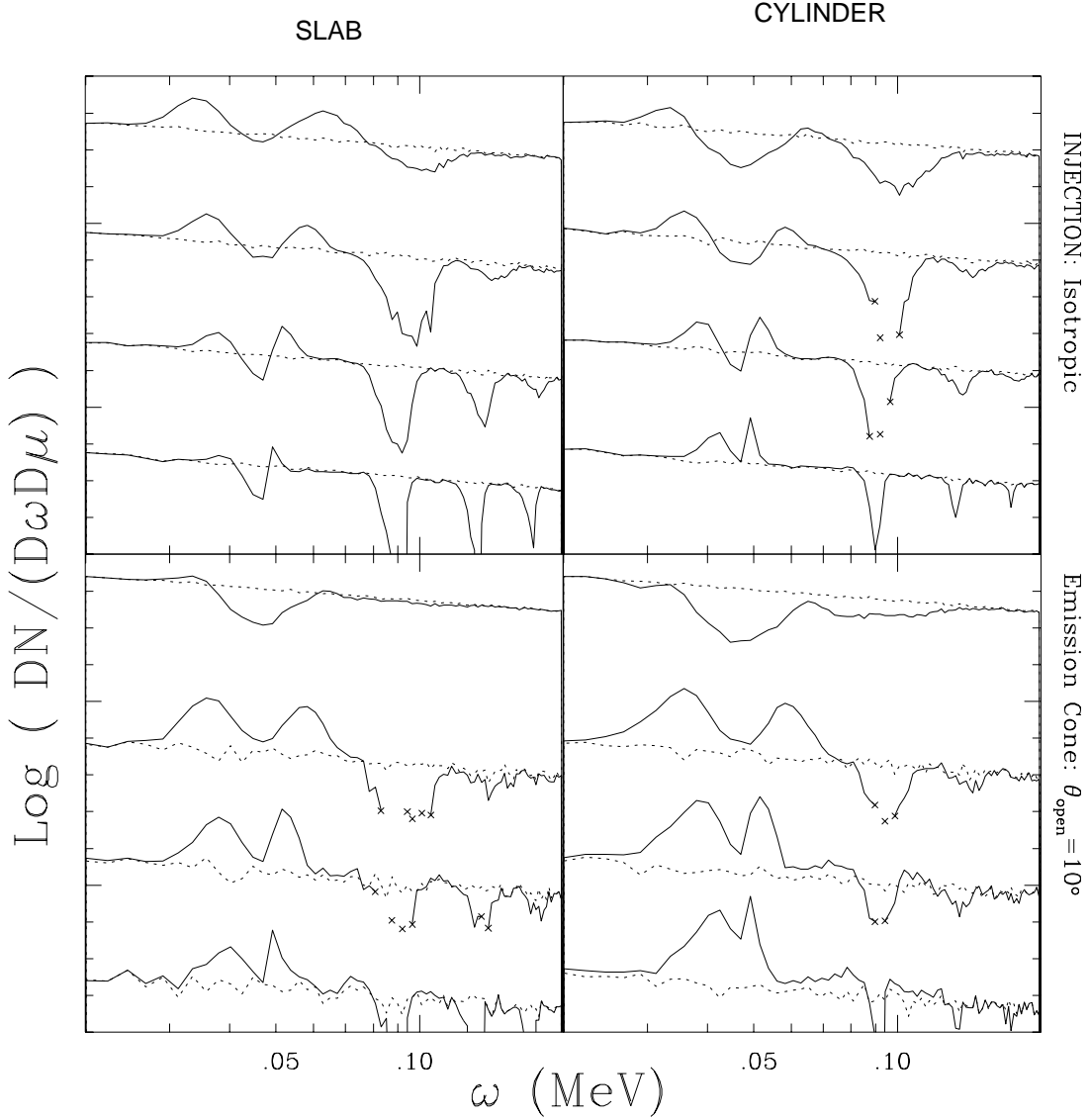


Fig. 5.— **Comparison between cone and isotropic injection for slab and cylindrical geometries.** The magnetic field strength is $B' = .1$ (4.414 TG). Each plot shows angle dependent model photon spectra. On each quadrant, the bottom plot is the spectrum emerging from $\mu < .25$, and the top plot shows the spectrum from $\mu > .75$, with similar binning in between. Each run has 50 thousand photons. Top plots correspond to isotropic injection, bottom plots to beamed injection, as previously described. **Dotted line:** injected continuum: power law with $\alpha = -1$. **Solid line:** output scattered spectrum. **Crosses:** areas where photon depletion has occurred. $\tau_c = 1 \times 10^{-3}$, $T_e = \frac{1}{4}\omega_{cyc}$ The flux normalization is arbitrary.

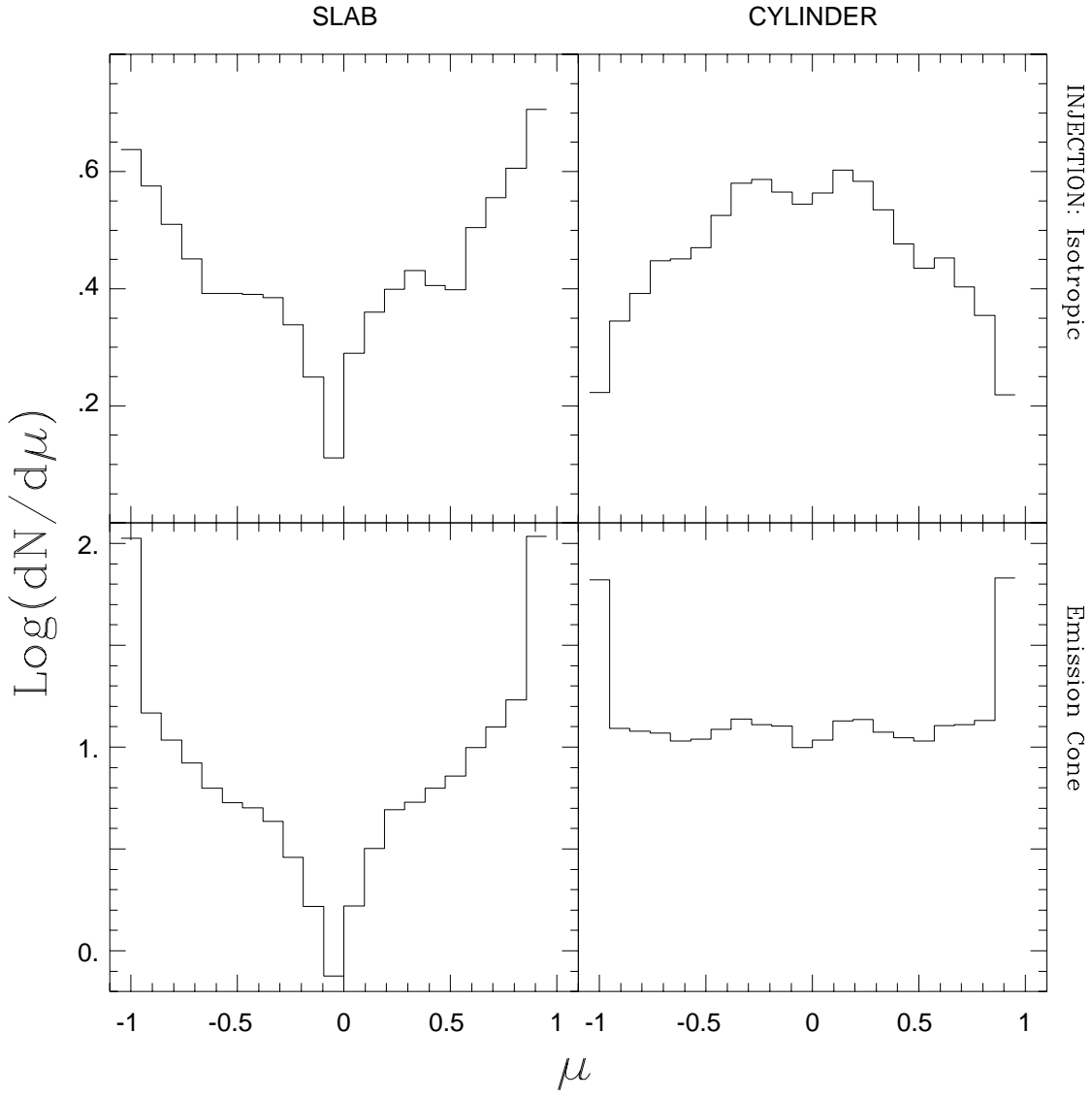


Fig. 6.— **Angular distribution comparison between cone and isotropic injection for slab and cylindrical geometries.** The parameters are identical with those of the preceding figure.

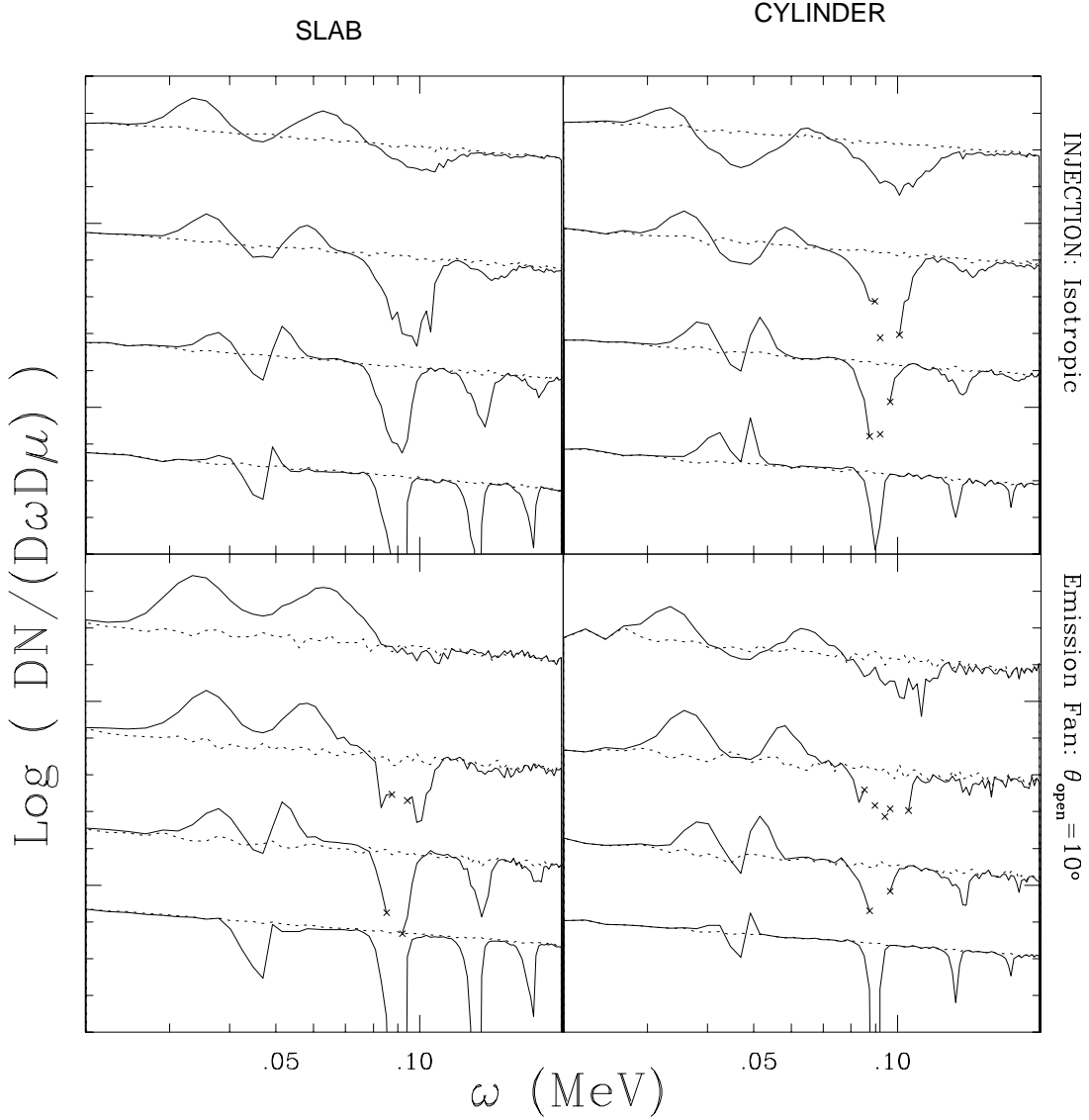


Fig. 7.— **Comparison between fan and isotropic injection for slab and cylindrical geometries.** The magnetic field strength is $B' = .1$ (4.414 TG). Each plot shows angle dependent model photon spectra. On each quadrant, the bottom plot is the spectrum emerging from $\mu < .25$, and the top plot shows the spectrum from $\mu > .75$, with similar binning in between. Each run has 50 thousand photons. Top plots correspond to isotropic injection, bottom plots to beamed injection, as previously described. **Dotted line:** injected continuum: power law with $\alpha = -1$. **Solid line:** output scattered spectrum. **Crosses:** areas where photon depletion has occurred. $\tau_c = 1 \times 10^{-3}$, $T_e = \frac{1}{4}\omega_{cyc}$. The flux normalization is arbitrary.

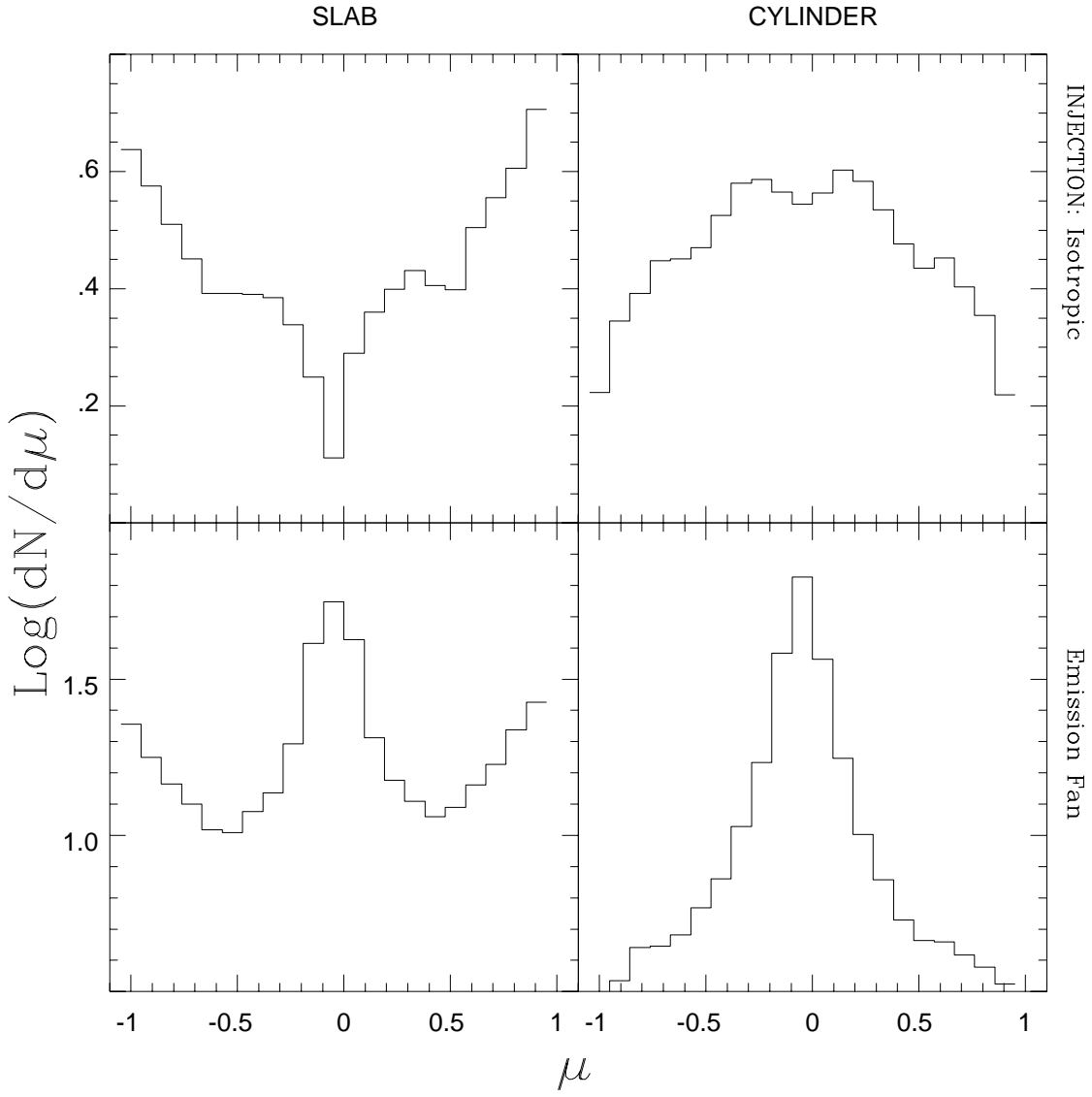


Fig. 8.— **Comparison of emergent angular distributions for fan and isotropic injections in slab and cylindrical geometries.** The parameters are identical with those of the preceding figure.

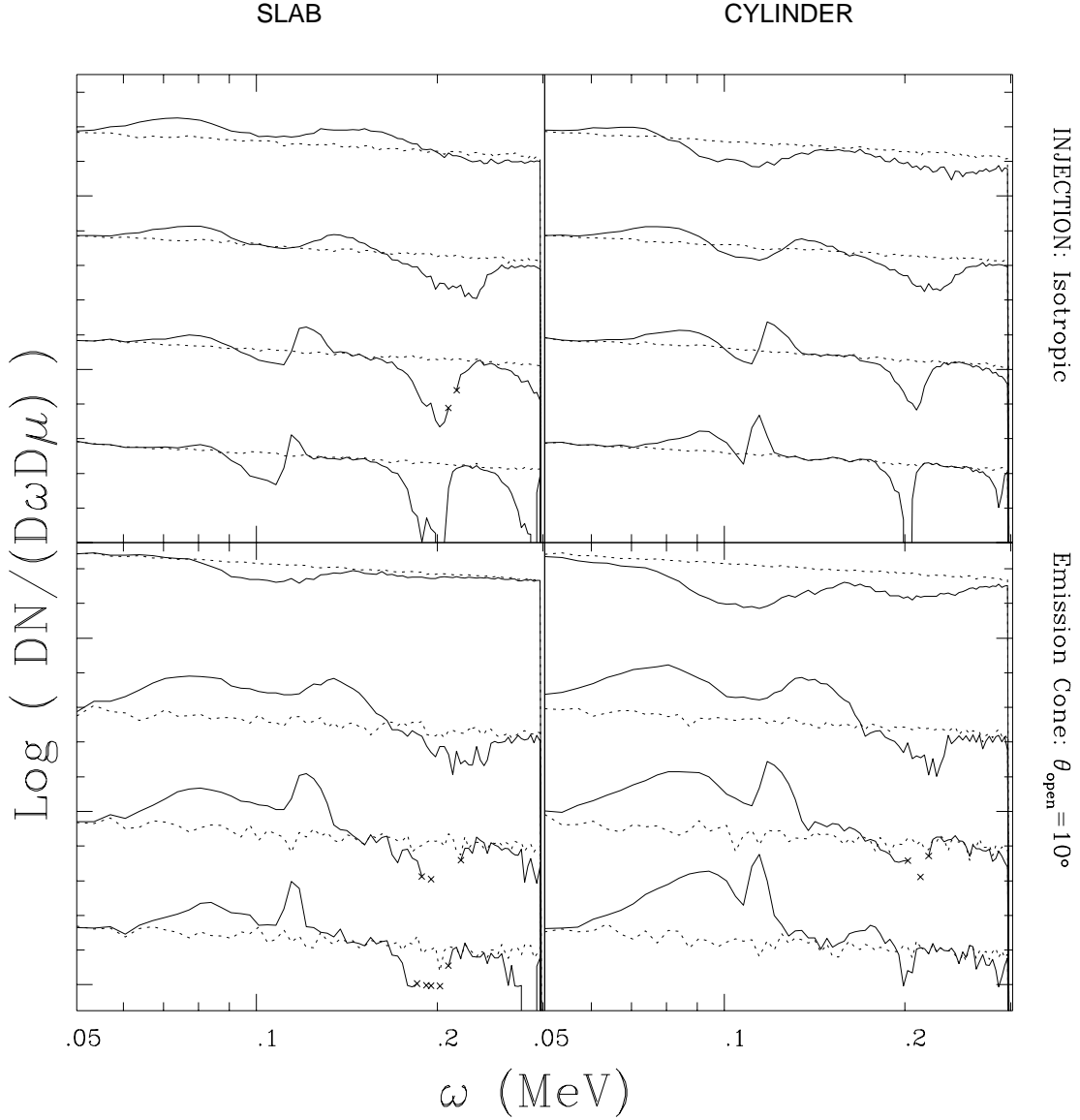


Fig. 9.— **Comparison between cone and isotropic injection for slab and cylindrical geometries.** The magnetic field strength is $B' = .2436$ (10.75 TG). Each plot shows angle dependent model photon spectra. On each quadrant, the bottom plot is the spectrum emerging from $\mu < .25$, and the top plot shows the spectrum from $\mu > .75$, with similar binning in between. Each run has 50 thousand photons. Top plots correspond to isotropic injection, bottom plots to beamed injection, as previously described. **Dotted line:** injected continuum: power law with $\alpha = -1$. **Solid line:** output scattered spectrum. **Crosses:** areas where photon depletion has occurred. $\tau_c = 1 \times 10^{-3}$, $T_e = \frac{1}{4}\omega_{cyc}$ The flux normalization is arbitrary.

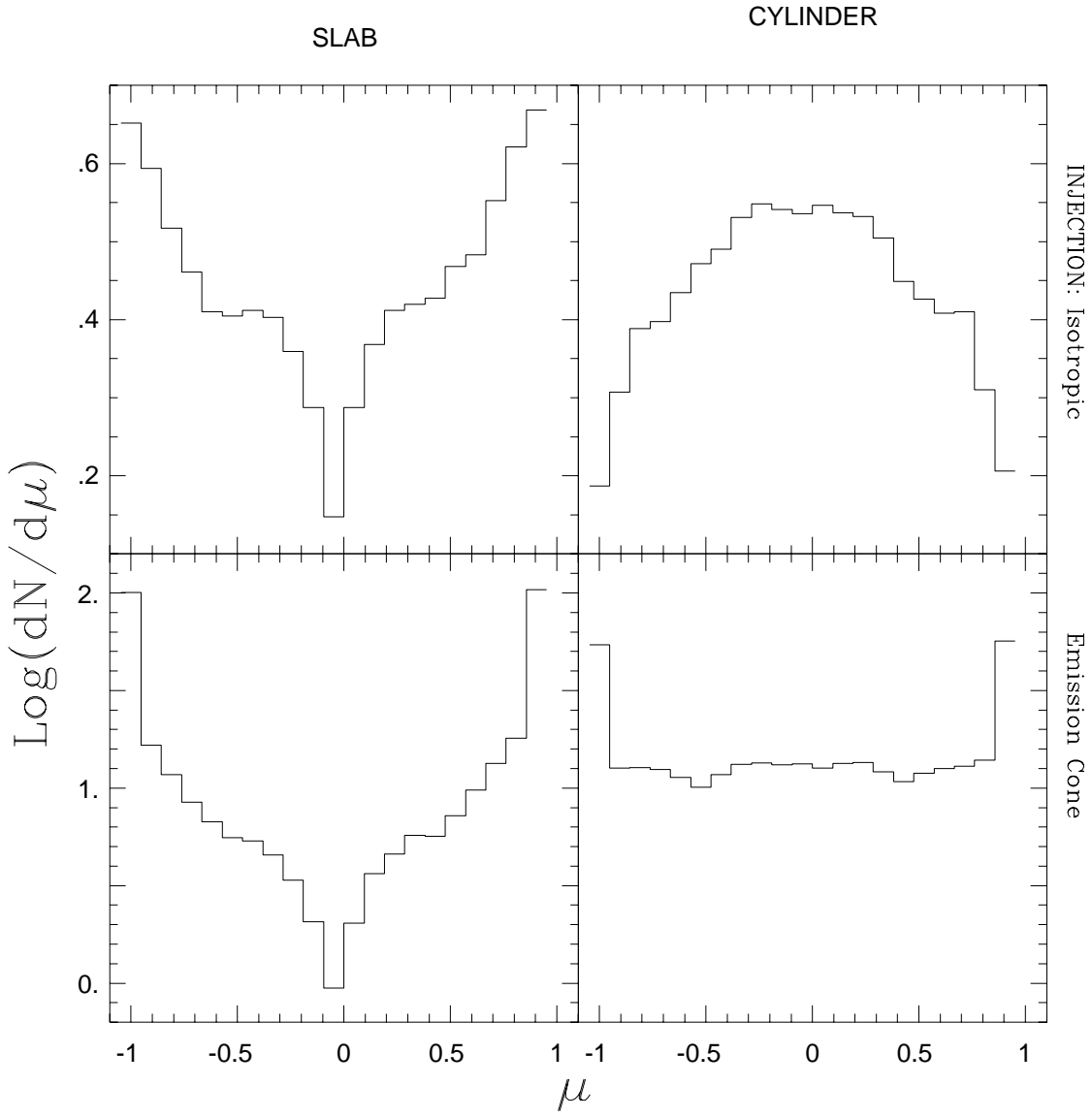


Fig. 10.— Comparison of emergent angular distributions for cone and isotropic injections in slab and cylindrical geometries. The parameters are identical with those of the preceding figure.

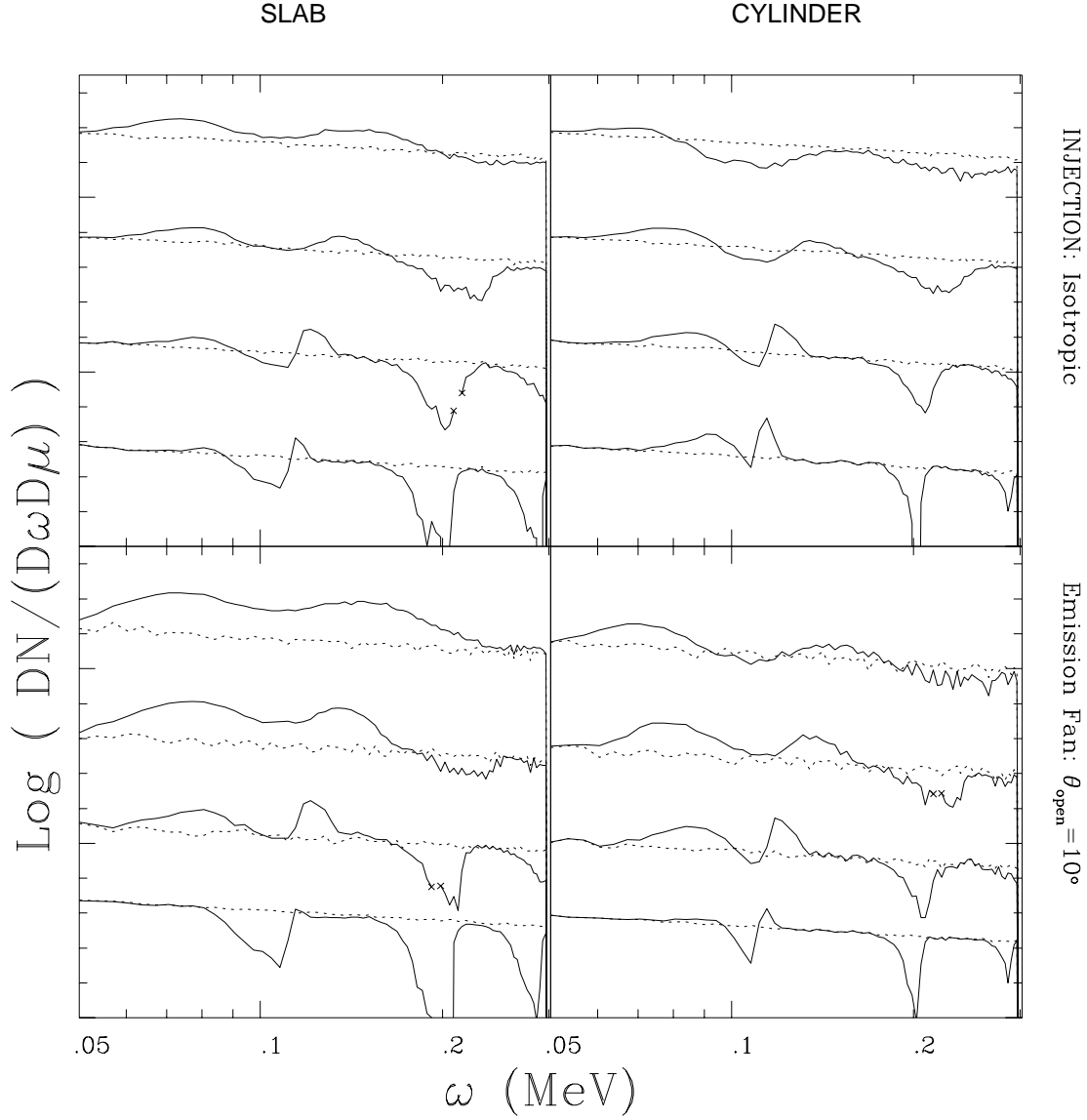


Fig. 11.— **Comparison between fan and isotropic injection for slab and cylindrical geometries.** The magnetic field strength is $B' = .2436$ (10.75 TG). Each plot shows angle dependent model photon spectra. On each quadrant, the bottom plot is the spectrum emerging from $\mu < .25$, and the top plot shows the spectrum from $\mu > .75$, with similar binning in between. Each run has 50 thousand photons. Top plots correspond to isotropic injection, bottom plots to beamed injection, as previously described. **Dotted line:** injected continuum: power law with $\alpha = -1$. **Solid line:** output scattered spectrum. **Crosses:** areas where photon depletion has occurred. $\tau_c = 1 \times 10^{-3}$, $T_e = \frac{1}{4}\omega_{cyc}$ The flux normalization is arbitrary.

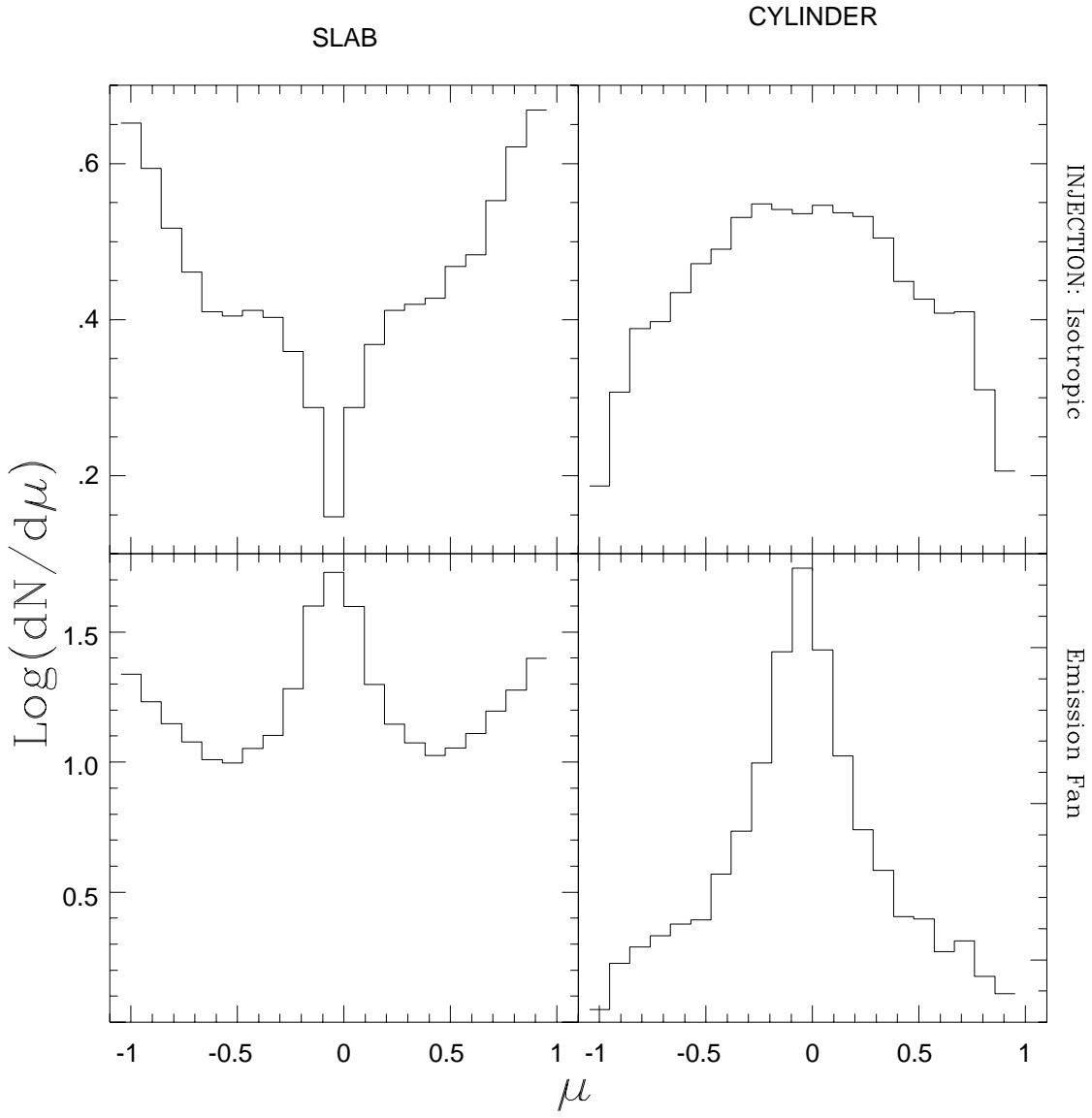


Fig. 12.— **Comparison of emergent angular distributions for fan and isotropic injections in slab and cylindrical geometries.** The parameters are identical with those of the preceding figure.